HOKKAIDO UNIVERSITY

Title	An electronic structure governed by the displacement of the indium site in In-S-6 octahedra: LnOInS(2) (Ln = La, Ce, and Pr)
Author(s)	Ito, Hiroaki; Miura, Akira; Goto, Yosuke; Mizuguchi, Yoshikazu; Moriyoshi, Chikako; Kuroiwa, Yoshihiro; Azuma, Masaki; Liu, Jinjia; Wen, Xiao-Dong; Nishioka, Shunta; Maeda, Kazuhiko; Masubuchi, Yuji; Rosero-Navarro, Nataly Carolina; Tadanaga, Kiyoharu
Citation	Dalton transactions, 48(32), 12272-12278 https://doi.org/10.1039/c9dt01562k
Issue Date	2019-08-28
Doc URL	http://hdl.handle.net/2115/79124
Type	article (author version)
Additional Information	There are other files related to this item in HUSCAP. Check the above URL.
File Information	LnOInS2-dalton-0709_AM F.pdf

Instructions for use

Hokkaido University Collection of Scholarly and Academic Papers : HUSCAP

Submitted manuscript: Dalton Transactions 2019, 48, 12272-12278

Electronic Structure Governed by Displacement of Indium Site in In–S_6 Octahedra: $LnOInS_2$ (Ln=La, Ce, and Pr)

Received 00th January 20xx,
Accepted 00th January 20xx

DOI: 10.1039/C9DT01562K

Hiroaki Ito[a], Akira Miura*[b], Yosuke Goto[c], Yoshikazu Mizuguchi[c], Chikako Moriyoshi[d], Yoshihiro Kuroiwa[d], Masaki Azuma[e], Jinjia Liu[f], Xiao-Dong Wen[f], Shunta Nishioka[g, h], Kazuhiko Maeda[g], Yuji Masubuchi[b], Nataly Carolina Rosero-Navarro[b], Kiyoharu Tadanaga[b]

Extremely large displacement of indium site in In–S_6 octahedra in $LnOInS_2$ (Ln=La, Ce, Pr) were found in synchrotron X-ray diffraction. $LaOInS_2$ with off-center indium in In–S_6 octahedra exhibited wider optical bandgap than those of $CeOInS_2$ and $PrOInS_2$ with on-center indium. Therefore, the electronic structure of $LnOInS_2$ is govern by the indium site with extremely large displacement. All the $LnOInS_2$ produced H_2 gas under visible light irradiation in the presence of sacrificial electron donors.

Introduction

Large atomic displacements from the equilibrium position in crystal structures are known to be key for designing functional materials such as thermoelectric materials,[1-4] superconductors,[5-7] electrodes,[8] and luminescent materials.[9] For example, suppression of thermal conductivity by large atomic displacements is an effective strategy for designing thermoelectric materials.[1-4] Large displacement of chalcogenide site in $BiCh_2$–superconductors is regarded as a key for emergence of superconductivity.[5-7] Conduction path in electrodes has been visualized by large atomic displacements.[8] Nonetheless, the effect of large atomic displacements on the electronic structure has not been fully understood by the experimental results. For instance, $12CaO•7Al_2O_3$ and $CoSb_3$ have cage structures, and have been extensively studied for use in developing various functional materials. H^- and In can be incorporated in these cage materials. H^- in $12CaO•7Al_2O_3$:H^- [10,11] and indium in $In_{0.125}Co_4Sb_{12}$[12,13] show large displacement in these cages, and hence are called as rattlers. The effect of these rattlers on their thermoelectric and electronic properties has been supported by computationally predicted electronic structures.[11,12] However, there is experimental difficulty to detect the states of these rattlers by X-ray photoemission spectroscopy (XPS). This is because the states contributed by these rattlers are much smaller than those by cages and the energy resolution of XPS is insufficient to distinguish between these contributions. Therefore, in order to design functional materials based on large atomic displacement, experimental study to bridge large displacement of atoms and its effect on the electronic structure is highly demanded.

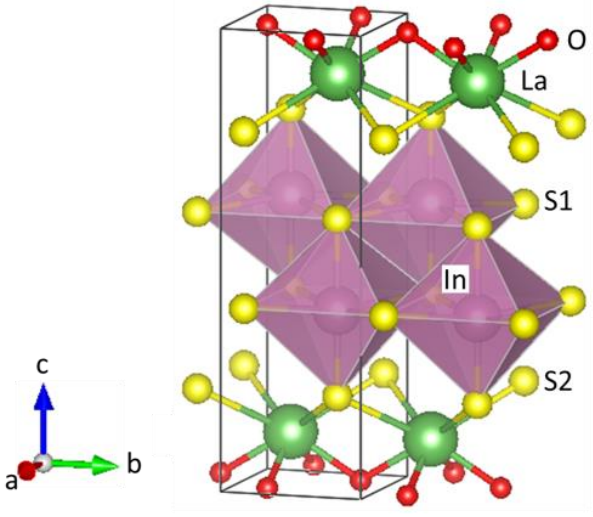

Figure 1 Crystal structure of $LaOInS_2$ drawn by VESTA.[14]

In order to experimentally examine the correlation between atomic displacement and electronic structure, it is desirable to synthesize compounds containing rattlers as major components whose atomic displacement can be rationally controlled. The layered oxysulfide $LaOInS_2$[15] would be a motif to examine the correlation between atomic displacement and electronic structures. Figure 1 shows the crystal structure of $LaOInS_2$.

[a] Graduate School of Chemical Sciences and Engineering, Hokkaido University, Kita 13, Nishi 8 Sapporo 060-8628, Japan.
[b] Faculty of Engineering, Hokkaido University, Kita 13, Nishi 8 Sapporo 060-8628, Japan.
[c] Department of Physics, Tokyo Metropolitan University, 1-1 Minami-osawa, Hachioji, Tokyo 192-0397, Japan.
[d] Department of Physical Science, Hiroshima University, 1-3-1 Kagamiyama, Higashihiroshima, Hiroshima 739-8526, Japan
[e] Materials and Structures Laboratory, Tokyo Institute of Technology, Yokohama 226-8503, Japan
[f] State Key Laboratory of Coal Conversion, Institute of Coal Chemistry, Chinese Academy of Sciences, Taiyuan 030001, P. R. China
[g] Department of Chemistry, School of Science, Tokyo Institute of Technology, 2-12-1-NE-2 Ookayama, Meguro-ku, Tokyo 152-8550, Japan
[h] Japan Society for the Promotion of Science, Kojimachi Business Center Building, 5-3-1 Kojimachi, Chiyoda-ku, Tokyo 102-0083, Japan

† Footnotes relating to the title and/or authors should appear here.
Electronic Supplementary Information (ESI) available: [details of any supplementary information available should be included here]. See DOI: 10.1039/x0xx00000x

Please do not adjust margins

$LaOInS_2$ has alternately stacked oxide and sulfide layers. The sulfide layer is composed of In–S_6 octahedra, and In in the octahedral cage exhibit large anisotropic displacement parameters. These large atomic displacements would be controlled by the substitution of lanthanum in the La–O layer with smaller rare-earth elements; the decrease in the ionic radius probably results in an increase in the chemical pressure applied on the In–S_6 octahedra[16,17]. Moreover, because indium is the major component of this compound and has a large scattering factor, synchrotron X-ray diffraction can help visualize the atomic displacement of indium in these compounds.

The electronic structure near the band gap of $LaOInS_2$ can be examined by their optical absorption. $LaOInS_2$ is reported to be a semiconductor photocatalyst with the band gap of ~2.64 eV. According to DFT calculations,[15] the sulfur 3p states are located near the valence band maximum, and the indium 5s and 5p states form the bottom of the conduction band. Thus, the electronic structure near the bottom of the conduction bands of $LaOInS_2$ and its isostructural analogs can be evaluated by optical absorption and reflect a large displacement of In. The electronic structure should be sensitive to the atomic displacement of indium, although XPS analysis is not suitable for examining the electronic structure because of the absorption species present on the surface of these compounds. [15]

In this study, we revealed the relationship between the electronic structure and large displacements by means of structural analysis and optical absorption experiments. The newly synthesized $CeOInS_2$ and $PrOInS_2$ were characterized and compared with $LaOInS_2$. The on-center indium in $CeOInS_2$ and $PrOInS_2$ shifted their optical absorption edge to a lower energy as compared with that corresponding to the off-center indium in $LaOInS_2$.

Results and discussion

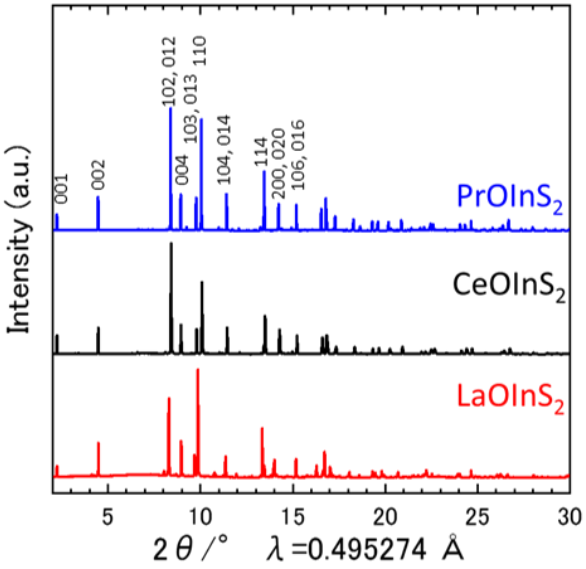

Figure 2 Synchrotron X-ray diffraction pattern of $LaOInS_2$, $CeOInS_2$, and $PrOInS_2$ at 300 K.

Layered oxysulfides $LnOInS_2$ (Ln=La, Ce, and Pr) were synthesized by the reaction of LnOCl and $NaInS_2$. Figure 2 indicates X-ray diffraction pattern of $LaOInS_2$, $CeOInS_2$, and $PrOInS_2$ at 300 K. Synchrotron X-ray diffraction results indicated that $CeOInS_2$ and $PrOInS_2$ were isostructural with monoclinic $LaOInS_2$.[15]

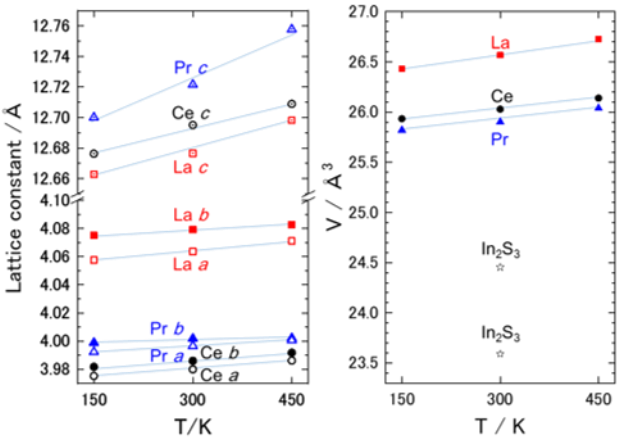

Figure 3 Temperature dependence of lattice constants *a*, *b*, and *c* and volume of In–S_6 octahedra of $LnOInS_2$. Two type of In–S_6 octahedra in In_2S_3 (ICSD-151644) are shown for comparison.

Rietveld refinement of synchrotron XRD data were performed for further structural analysis. Even though only monoclinic cell can be fit with atomic positions of $LnOInS_2$, the refinements of β converged with 90° within the error. Therefore, all the $LnOInS_2$ were refined as monoclinic phases but β was fixed as 90°, according to the previous report about $LaOInS_2$.[15] Since indium is a heavy atom and has a large atomic scattering factor, its probability density function of indium in $LnOInS_2$ can be determined. For initial Rietveld refinements of XRD patterns of $LnOInS_2$, the position of indium was settled in the central position of In–S_6 octahedral cage and second-order (harmonic) displacement parameters of indium (U_{11}, U_{22}, and U_{33}) were assumed, and U_{12}, U_{13}, and U_{23} were fixed as zero. These refinements converged with moderate refinement factors (R_{wp}); $LaOInS_2$: 8.58%, $CeOInS_2$: 9.88 %, and $PrOInS_2$: 9.29 % and derived larger thermal displacement of indium than that of the other atoms. Since U_{22} was extremely large for $LaOInS_2$ and $PrOInS_2$, In was expected to possess large atomic displacement along the *b* axis. In order to depict large atomic displacement of In, anharmonic displacement model was introduced. In this crystal structure model, indium was fixed at the central position of the In–S_6 Octahedron, and a fourth-order (anharmonic) atomic displacement parameter,[18] D_{2222}, represented the thermal displacement of indium along the *b* axis. Rietveld refinements of the XRD patterns of $LaOInS_2$ and $PrOInS_2$, with fourth-order displacement parameter of indium, improved the refinement factors ($LaOInS_2$: 8.27 % and $PrOInS_2$: 9.24 %). Split models with two In sites were also employed for $LaOInS_2$ and $PrOInS_2$. The details of the refinements with site split and anharmonic displacement models are summarized in supporting document. These models suggested that the atomic position derived by these two-site model were same as the position of maximum probability density derived by the model

This journal is © The Royal Society of Chemistry 20xx

Please do not adjust margins

with fourth-order (anharmonic) atomic displacement parameter. Thus, we conclude that both models are comparable although here we explained the results by using the model with anharmonic atomic displacements. On the other hand, for $CeOInS_2$, the refinement of XRD pattern with harmonic displacement parameters converged with U less than 0.1 $Å^2$. Furthermore, the fourth-order term D_{2222} converged with negative probability density although its refinement factor improved. The position of In with the split model of $CeOInS_2$ converged into central position of In–S_6 octahedra within the statistic error. Thus, the XRD pattern of $CeOInS_2$ was refined by a simple model without the fourth-order atomic displacement parameters and split In site.

Figure 3 shows the temperature dependence of lattice constants. The Rietveld profiles of $LaOInS_2$, $CeOInS_2$, and $PrOInS_2$ are shown in Figure S2. The details of the refinement are summarized in Table S2, Table S3, and Table S4. The lattice constants a and b decreased upon the substitution of La by Ce and Pr, while the lattice constant c increased. A decrease in temperature from 450 K to 300 and 150 K decreased the lattice constants and increased the difference between the lattice constants a and b. The volume of In–S_6 octahedron is also shown in Figure 3. This volume was significantly larger than those of In–S_6 octahedra found in In_2S_3 (ICSD-151644), indicating that octahedral cages were expanded by Ln–O layers.

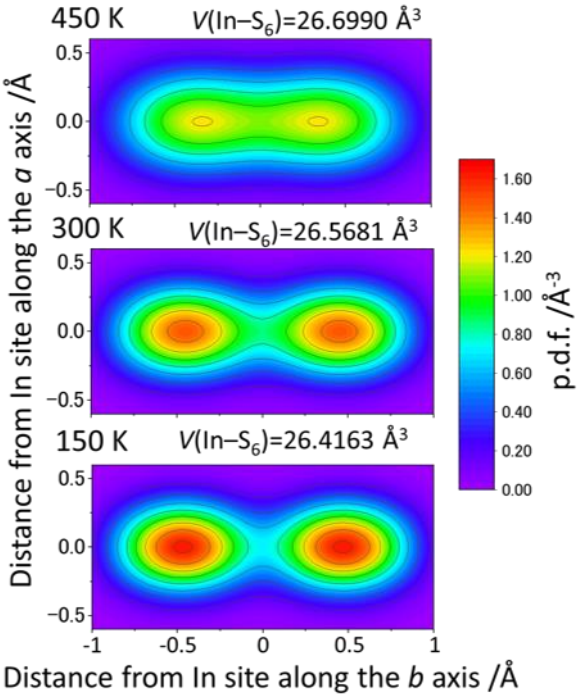

Figure 4 Probability density functions of indium in the *ab* plane of $LaOInS_2$ at 150, 300, and 450 K were derived from the Rietveld analysis using Jana2006 program.[19] V(In–S_6) represents the volume of In–S_6 octahedra.

Figure 4 shows the crystal structure and the probability density function of indium in the *ab* plane of $LaOInS_2$. The probability density functions of indium between 150 and 450 K showed two maxima at the off-center positions and a local minimum at the center of the In–S_6 octahedra. As the temperature decreased from 450 to 150 K, the volume of the In–S_6 octahedra decreased by approximately 1.1 %. The decrease in temperature increased the distance between the center and the maxima from 0.34 to 0.46 Å, and decreased the probability density at the center from 1.11 to 0.72 $Å^{-3}$. Assuming that the magnitude of atomic displacement continuously changes with temperature, indium can be expected to exhibit a large atomic displacement even at 0 K. Hence, the atomic displacement parameters for indium are anomalous.[15] Larger atomic displacement of In in $LaOInS_2$ was also supported by In K–edge X-ray Absorption Fine Structure (XAFS) (Figure S6). The probability density functions of $CeOInS_2$ and $PrOInS_2$ at 150, 300, and 450 K are shown in Figure S3 and Figure S4, respectively. The probability density function of $PrOInS_2$ at 450 K showed one maximum at the center of the In–S_6 octahedra. At 150 and 300 K, the functions had two maximum points, and the maxima were slightly off-centered at lower temperature. In $CeOInS_2$, the probability density function of indium at the center of the In–S_6 octahedra was the maximum in the temperature range between 150 and 450 K. The indium atoms in $CeOInS_2$ and $PrOInS_2$ were also considered to show large displacement even at 0 K. In other words, we found abnormal displacements of indium in $LaOInS_2$, $CeOInS_2$, and $PrOInS_2$.

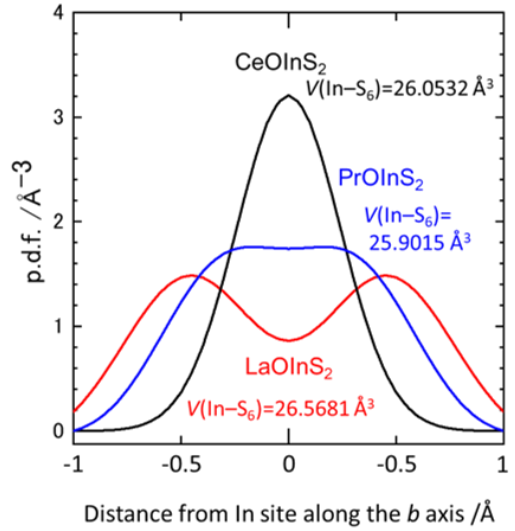

Figure 5 Probability density functions of indium in $LaOInS_2$, $CeOInS_2$, and $PrOInS_2$ along the *b* axis and volumes of In–S_6 octahedra.

Figure 5 shows the probability density functions along the *b* axis of $LaOInS_2$, $CeOInS_2$, and $PrOInS_2$ at 300 K. The probability density of indium at the center of the In–S_6 octahedra in $LaOInS_2$ was located at the off-center positions, whereas the probability densities at the center of the In–S_6 octahedra were the maximum in $CeOInS_2$. The probability density at the center in $PrOInS_2$ was close to maximum although two maximums appeared in off-center positions. Higher probability density in off-center position can be understood by longer lattice parameter of *b*-axis (Figure 3: $CeOInS_2$<$PrOInS_2$<<$LaOInS_2$). The distance from sulfur to center of the In–S_6 octahedron on *ab* plane were 2.8895(4) Å for $LaOInS_2$, 2.8235(3) Å for $CeOInS_2$, and 2.8406(3) Å for $PrOInS_2$. These distance are much larger than the sum of ionic radii of In^{3+} and S^{2-} (2.64 Å), and shifting of In atom from the center of octahedron would be favorable to

Please do not adjust margins

shorter bond lengths between In and S. Similar shifting of Bi^{3+} are also proposed in structurally-related $LaOBiS_2$ and LaOBiSSe.[20]

Although ionic radius of Ce^{3+} is larger than Pr^{3+},[21] the lattice parameters *a* and *b* of $CeOInS_2$ were shorter than that of $PrOInS_2$. In order to explain these results, the valence state of Ce was examined by XAFS. The Ce L_3–edge XAFS spectra of $CeOInS_2$ is shown in Figure 6. Although Ce^{3+} was dominant in $CeOInS_2$, Ce^{4+} was also detected. The fraction of Ce^{4+} was estimated to be 10 % from linear combination fitting of the spectra of Ce_2S_3 and CeO_2. Since the ionic radius of Ce^{4+} is smaller than that of Ce^{3+} and Pr^{3+},[21] the smaller lattice constants *a* and *b* of $CeOInS_2$ than those of $PrOInS_2$ can be explained by the existence of Ce^{4+}.

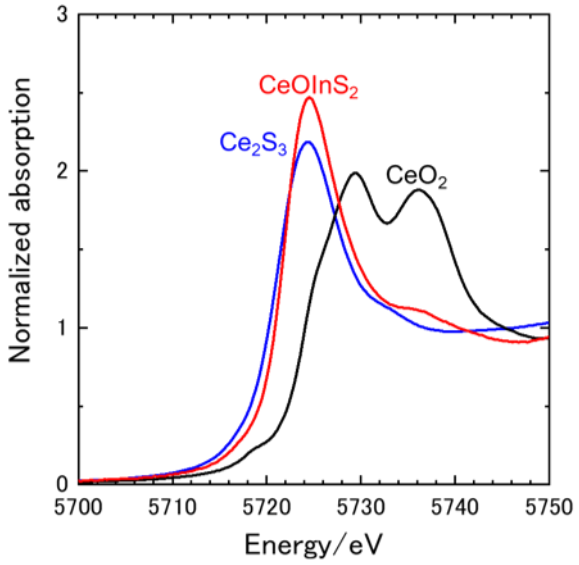

Figure 6 Ce L_3–edge XAFS spectra of $CeOInS_2$. Ce_2S_3 and CeO_2 are references of Ce^{3+} and Ce^{4+} cation, respectively.

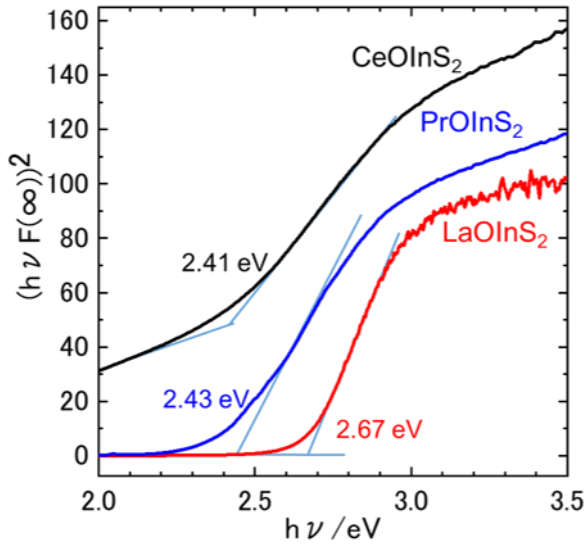

Figure 7 Tauc plot of diffuse reflectance of $LnOInS_2$ at 300 K.

Figure 7 shows the Tauc plots derived from diffuse reflectance measurements of $LnOInS_2$ at 300 K by assuming their direct transition. The optical absorption gaps of $LaOInS_2$, $CeOInS_2$, and $PrOInS_2$ were determined to be 2.67, 2.41, and 2.43 eV, respectively.

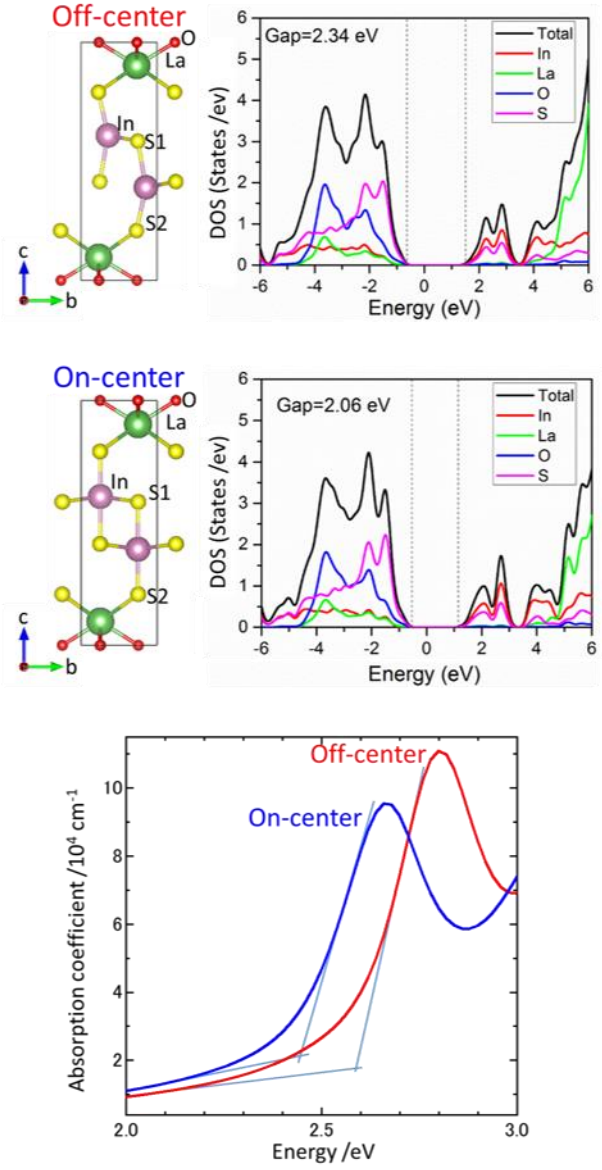

Figure 8 Crystal structure models of $LaOInS_2$, electronic structures, and absorption coefficients calculated by the DFT method.

The probability density of indium in $LaOInS_2$ was low at the center of the In–S_6 octahedra and spread along the *b* axis, while that in $CeOInS_2$ and $PrOInS_2$ was distributed at the center of the In–S_6 octahedra. The optical absorption gap of $LaOInS_2$ was approximately 0.3 eV larger than that of $CeOInS_2$ and $PrOInS_2$. These differences suggest that optical absorption of $LnOInS_2$ is controlled by the atomic displacement of indium. The influence of the displacement of indium on absorption was also investigated by density functional theory (DFT) calculation. The split models with the on-center or off-center indium sites in the

This journal is © The Royal Society of Chemistry 20xx

Please do not adjust margins

Please do not adjust margins

In–S_6 octahedra were used. Figure S7 and Table S7 show the structure models with several arrangements of indium atoms and the calculation results, respectively. We assumed the static distribution of indium in several models. XRD only reflects the average structure, so the statistic or dynamic displacement has not been clarified. Although DFT calculations supported the fact that the optical absorption is sensitive to the indium position as below, these calculations were based on structural models with limited supercells. The ordering of the indium positions and dynamics of indium would also affect the electronic structure, and further study in this regard is necessary. Nonetheless, the results showed that the bandgaps depend on the position of indium. The simulation models, electronic structures, and absorption coefficients are shown in Figure 8. The PBE-GGA method was employed for structure optimization, and the HSE06 method was used for the calculation of the electronic structure and absorption coefficients. The electronic structure of the on-center and off-center models were similar, and the valence band maximum and conduction band minimum were all dominated by sulfur and indium, respectively. The energy level of absorption edge of the model with off-center indium sites was 2.60 eV, which was 0.15 eV higher than that of on-center model. In both models, the bond between indium and the nearest sulfur was parallel to the *c* axis. Furthermore, the hybridization of the indium 5p and sulfur 3p orbitals was decreased by the displacement of indium. Consequently, the energy difference of the hybridized orbitals increased and the optical absorption edge, which corresponds to the band edge, shifted toward shorter wavelengths.

Experimental results showed that the probability densities of indium at the center of the In–S_6 octahedra in $LaOInS_2$ were lower, and the optical band gaps were about 0.3 eV wider than that of $CeOInS_2$ and $PrOInS_2$. Computational results showed that the absorption edge of $LaOInS_2$ was affected by the thermal displacement of indium in the In–S_6 octahedra; the off-center models showed an absorption edge with higher energy than the center models. These results indicate that the optical absorption of $LnOInS_2$ can be modulated by the large thermal displacement of indium. Synchrotron X-ray diffraction showed that the potential curve for indium in $LaOInS_2$ had two minima at the off-center positions that were about 0.5 Å apart from the center of the In–S_6 octahedra. The energy barrier between two off-center positions was about 14 meV (Figure S5). Since the product of the Boltzmann constant and temperature at 300 K (25 meV) is higher than the energy barrier, indium would dynamically move between the two off-center positions. Although further investigation of dynamic displacement is necessary, our results show that $LaOInS_2$ is a suitable motif to show the correlation between atomic displacement and electronic properties and help us understand how the atomic displacement affects the properties of solid-state compounds.

Finally, photocatalytic activities of $LnOInS_2$ for H_2 evolution were examined. As shown in Figure 9, all of the $LnOInS_2$ produced H_2 upon visible light. The amount of H_2 evolved from the Pt–loaded $CeOInS_2$ and $PrOInS_2$ samples were less than 10% of that from Pt–loaded $LaOInS_2$ sample. The lower activities of Ce- and Pr-analogues may be explained by the existence of 4f electrons, which can increase the electron-hole recombination rates.[2223].

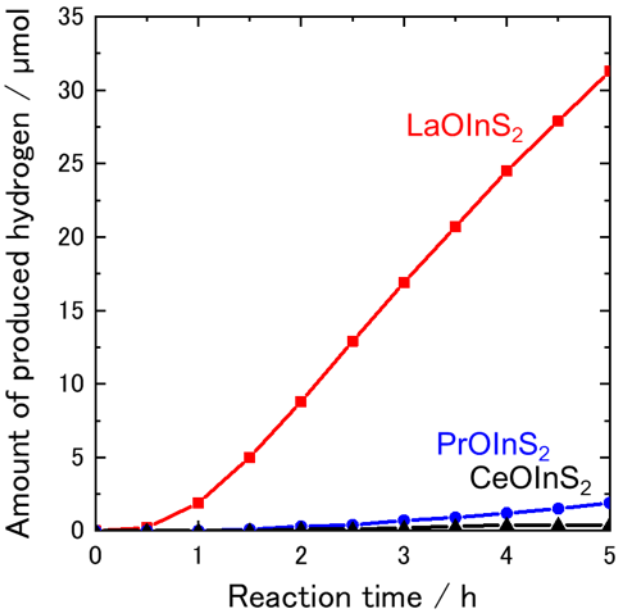

Figure 9 Time courses of H_2 evolution on Pt-loaded $LnOInS_2$ under visible light irradiation ($420 < \lambda < 800$ nm). Reaction conditions: catalyst, 50 mg; aqueous Na_2S (10 mM) + Na_2SO_3 (10 mM) solution; light source, xenon lamp (300 W) with a cutoff filter (L-42); reaction vessel, Pyrex top-irradiation type.

Conclusions

In summary, we found that the optical absorption correlated with the electronic structure of $LnOInS_2$ depended on the abnormally high displacement of indium. The probability density function of indium at the center of In–S_6 octahedra was low in $LaOInS_2$, but high in $CeOInS_2$ and $PrOInS_2$. The optical band gap of $LaOInS_2$ was about 0.3 eV wider than that of $CeOInS_2$ and $PrOInS_2$. The optical absorption was demonstrated to be sensitive to the indium position by computational calculations. These experimental and computational results confirm the electronic structure modulation by the atomic displacements of indium, and will deepen our understanding toward the development of new functionalities controlled by atomic displacement.

Experimental

Synthesis

$LnOInS_2$ was synthesized from $NaInS_2$ and LnOCl. $NaInS_2$ was obtained by heating $NaSH{\cdot}nH_2O$ (Sigma-Aldrich) and $In(NO_3)_3{\cdot}nH_2O$ (Kanto Chemical) at 200 °C in a Teflon-coated autoclave. LnOCl was prepared by heating of lanthanoid

This journal is © The Royal Society of Chemistry 20xx

Please do not adjust margins

Please do not adjust margins

chlorides at 650–820 °C for 34 h. $LaCl_3 \cdot 7H_2O$ (Wako) and $PrCl_3 \cdot 7H_2O$ (Junsei Chemical) were heated in a flow of N_2. $CeCl_3 \cdot 7H_2O$ (Junsei Chemical) was heated in a flow of H_2 (4%) and Ar. Then, $LnOInS_2$ was synthesized in an evacuated quartz tube by the metathesis reaction of LnOCl and $NaInS_2$ at 850 °C. After cooling, the obtained powders were washed by distilled water to remove the NaCl byproduct.

Characterization

Synchrotron X-ray diffraction profiles were measured at 150, 300, and 450 K at the BL02B2 beam line at SPring-8 (Proposal Numbers: 2017B1211, 2018A0074, 2018B1246, and 2019A1114). The wavelength of the incident X-ray used for presented refinements was 0.495274 Å. The diffraction data was collected using a high-resolution one-dimensional semiconductor detector, multiple MYTHEN system.[24] The X-ray diffraction data were analyzed by the Rietveld method using the Jana2006 program,[19] and the crystal structure was drawn using the VESTA program.[14] We depicted the probability density function of *ab* plane locating indium site, which is averaged along the *c* axis in the range of 0.8 Å with 0.05 Å intervals. The potential curves for indiums in $LaOInS_2$ and $PrOInS_2$ were calculated from respective probability density functions.[25] The valence of cerium was estimated by X-ray absorption fine structure (XAFS) spectroscopy analysis at the beam line BL11S2 of Aichi Synchrotron Radiation Center (Proposal Number: 201801025). The diffuse reflectance spectra of $LnOInS_2$ were measured from 200 nm to 850 nm using a UV-vis spectrophotometer (JASCO V-750) at room temperature. The optical band gaps of $LaOInS_2$, $CeOInS_2$, and $PrOInS_2$ were calculated assuming their direct band gaps.

Computational

Projected density of states (pDOS) and optical absorption coefficient were calculated by density functional theory (DFT) using the VASP package[26,27] with the PBE and HSE06 method[28,29] the projector augmented wave (PAW) method[30] with energy cutoff of 400 eV were utilized. The convergence criteria for all calculations set for the electronic self-consistent iterations and forces with 10^{-5} eV and 0.02 eV/Å respectively. The Gama-point-centered Monkhorst–Pack (MP) (5×5×2) k-mesh scheme[31] was employed for structure optimization and density of states (DOS) and dielectric function calculations. The imaginary part ($\varepsilon Im(\omega)$) of the frequency dependent dielectric matrix (ε) is determined for the calculation of absorption coefficient and bandgaps by a summation over empty states using the converged ground state.[15]

Photocatalytic reactions

Photocatalytic H_2 evolution reaction was conducted at room temperature using a top-irradiation type cell that was connected to a closed gas circulation system made of glass. 50 mg of sample was dispersed in aqueous Na_2S (10 mM) and Na_2SO_3 (10 mM) mixed solution (140 mL). A Pt cocatalyst (0.75 wt%) was loaded onto $LnOInS_2$ by an in-situ photodeposition method using $H_2PtCl_6 \cdot 6H_2O$ (Kanto Chemical) as the precursor. After outgassing the reactant solution by a vacuum pump, Ar gas (ca. 5 kPa) was introduced into the reaction system and the solution was irradiated under a 300 W Xe lamp (Cermax, PE300BF) with an output current of 20 A. The irradiation wavelength was fitted by the combination of a cold mirror (CM-1), cutoff filter (L-42) and water filter (λ > 420 nm). The evolved gases during the preparation process were analysed by a gas chromatography (GL Sciences, GC–3200 with TCD detector; argon carrier gas).

Conflicts of interest

There are no conflicts to declare.

Acknowledgements

This work was partly supported by Grants-in-Aid for Scientific Research (Nos. JP16H04493, JP16H06439, JP16H06441, JP19H04682).

Notes and references

1 Sales, B. C., Mandrus, D. & Williams, R. K. Filled Skutterudite Antimonides: A New Class of Thermoelectric Materials. *Science* **272**, 1325-1328, doi:10.1126/science.272.5266.1325 (1996).

2 Fujiwara, A. *et al.* Quantitative relation between structure and thermal conductivity in type-I clathratesX8Ga16Ge30(X=Sr, Ba) based on electrostatic-potential analysis. *Phys. Rev. B* **85**, doi:10.1103/PhysRevB.85.144305 (2012).

3 Mizuguchi, Y. *et al.* Compositional and temperature evolution of crystal structure of new thermoelectric compound $LaOBiS_{2-x}Se_x$. *J. Appl. Phys.* **119**, 155103, doi:10.1063/1.4946836 (2016).

4 Suekuni, K. *et al.* Retreat from Stress: Rattling in a Planar Coordination. *Adv. Mater.* **30**, e1706230, doi:10.1002/adma.201706230 (2018).

5 Hattori, K. & Tsunetsugu, H. Strong coupling superconductivity mediated by three-dimensional anharmonic phonons. *Phys. Rev. B* **81**, doi:10.1103/PhysRevB.81.134503 (2010).

6 Nagasaka, K. *et al.* Intrinsic Phase Diagram of Superconductivity in the $BiCh_2$-Based System Without In-Plane Disorder. *J. Phys. Soc. Jpn.* **86**, 074701, doi:10.7566/jpsj.86.074701 (2017).

7 Mizuguchi, Y. *et al.* Evolution of Anisotropic Displacement Parameters and Superconductivity with Chemical Pressure in BiS_2-Based $REO_{0.5}F_{0.5}BiS_2$ (RE = La, Ce, Pr, and Nd). *J. Phys. Soc. Jpn.* **87**, 023704, doi:10.7566/jpsj.87.023704 (2018).

8 Nishimura, S.-i. *et al.* Experimental visualization of lithium diffusion in LixFePO4. *Nat Mater* **7**, 707-711 (2008).

9 Jin, M., Chung, T. S., Seki, T., Ito, H. & Garcia-Garibay, M. A. Phosphorescence Control Mediated by Molecular Rotation and Aurophilic Interactions in Amphidynamic Crystals of 1,4-Bis[tri-(p-fluorophenyl)phosphane-gold(I)-ethynyl]benzene. *J.*

 This journal is © The Royal Society of Chemistry 20xx

Please do not adjust margins

Please do not adjust margins

Am. Chem. Soc. **139**, 18115-18121, doi:10.1021/jacs.7b11316 (2017).

10 Hayashi, K., Matsuishi, S., Kamiya, T., Hirano, M. & Hosono, H. Light-induced conversion of an insulating refractory oxide into a persistent electronic conductor. *Nature* **419**, 462, doi:10.1038/nature01053 (2002).

11 Ikeda, T. First principles centroid molecular dynamics simulation of hydride in nanoporous C12A7:H−. *The Journal of Chemical Physics* **146**, 204503, doi:10.1063/1.4983707 (2017).

12 Zhao, W. *et al.* Multi-localization transport behaviour in bulk thermoelectric materials. *Nature Communications* **6**, 6197, doi:10.1038/ncomms7197 (2015).

13 Zhao, W. *et al.* Enhanced Thermoelectric Performance in Barium and Indium Double-Filled Skutterudite Bulk Materials via Orbital Hybridization Induced by Indium Filler. *J. Am. Chem. Soc.* **131**, 3713-3720, doi:10.1021/ja8089334 (2009).

14 Momma, K. & Izumi, F. VESTA: a three-dimensional visualization system for electronic and structural analysis. *J. Appl. Crystallogr.* **41**, 653-658, doi:doi:10.1107/S0021889808012016 (2008).

15 Miura, A. *et al.* Synthesis, structure and photocatalytic activity of layered $LaOInS_2$. *Journal of Materials Chemistry A* **5**, 14270-14277, doi:10.1039/c7ta04440b (2017).

16 Mizuguchi, Y. *et al.* In-plane chemical pressure essential for superconductivity in $BiCh_2$-based (Ch: S, Se) layered structure. *Scientific Reports* **5**, 14968, doi:10.1038/srep14968 (2015).

17 Miura, A. *et al.* Crystal Structure and Superconductivity of Tetragonal and Monoclinic $Ce_{1-x}Pr_xOBiS_2$. *Inorg. Chem.* **57**, 5364-5370, doi:10.1021/acs.inorgchem.8b00349 (2018).

18 Trueblood, K. N. *et al.* Atomic Dispacement Parameter Nomenclature. Report of a Subcommittee on Atomic Displacement Parameter Nomenclature. *Acta Crystallographica Section A* **52**, 770-781, doi:10.1107/S0108767396005697 (1996).

19 Petříček, V., Dušek, M. & Palatinus, L. Crystallographic Computing System JANA2006: General features. *Z. Kristallogr.* **229**, 345, doi:10.1515/zkri-2014-1737 (2014).

20 K. Terashima *et al.* Enhanced thermoelectricity by controlled local structure in bismuth-chalcogenides. *J. Appl. Phys.* **125**, 145105, doi:10.1063/1.5087096 (2019).

21 Shannon, R. D. Revised effective ionic radii and systematic studies of interatomic distances in halides and chalcogenides. *Acta Crystallographica Section A* **32**, 751-767 (1976).

22 Machida, M., Murakami, S., Kijima, T., Matsushima, S. & Arai, M. Photocatalytic Property and Electronic Structure of Lanthanide Tantalates, LnTaO4 (Ln = La, Ce, Pr, Nd, and Sm). *The Journal of Physical Chemistry B* **105**, 3289-3294, doi:10.1021/jp004297z (2001).

23 Wakayama, H. *et al.* Synthesis of a Layered Niobium Oxynitride, Rb2NdNb2O6N·H2O, Showing Visible-Light Photocatalytic Activity for H2 Evolution. *Inorg. Chem.* **58**, 6161-6166, doi:10.1021/acs.inorgchem.9b00414 (2019).

24 Kawaguchi, S. *et al.* High-throughput powder diffraction measurement system consisting of multiple MYTHEN detectors at beamline BL02B2 of SPring-8. *Rev. Sci. Instrum.* **88**, 085111, doi:10.1063/1.4999454 (2017).

25 Kiat, J.-M. *et al.* Anharmonicity and disorder in simple and complex perovskites: a high energy synchrotron and hot neutron diffraction study. *J. Phys.: Condens. Matter* **12**, 8411-8425, doi:10.1088/0953-8984/12/39/305 (2000).

26 Kresse, G. & Furthmüller, J. Efficient iterative schemes for ab initio total-energy calculations using a plane-wave basis set. *Phys. Rev. B* **54**, 11169-11186 (1996).

27 Kresse, G. & Hafner, J. Ab initio molecular dynamics for liquid metals. *Phys. Rev. B* **47**, 558-561 (1993).

28 Heyd, J. & Scuseria, G. E. Efficient hybrid density functional calculations in solids: Assessment of the Heyd–Scuseria–Ernzerhof screened Coulomb hybrid functional. *The Journal of Chemical Physics* **121**, 1187-1192, doi:10.1063/1.1760074 (2004).

29 Perdew, J. P., Burke, K. & Ernzerhof, M. Generalized Gradient Approximation Made Simple. *Phys. Rev. Lett.* **77**, 3865-3868 (1996).

30 Blöchl, P. E. Projector augmented-wave method. *Phys. Rev. B* **50**, 17953-17979 (1994).

31 Monkhorst, H. J. & Pack, J. D. Special points for Brillouin-zone integrations. *Phys. Rev. B* **13**, 5188-5192 (1976).

Please do not adjust margins